


Structural Insights into Two Representative Conformations of the Complex Formed by *Grapholita molesta* (Busck) Pheromone Binding Protein 2 and Z-8-Dodecenyl Acetate

Zhen Tian,^{†,‡} Yue Li,[†] Yijia Xing,[‡] Ruichi Li,[†] and Jiyuan Liu^{*,†} 

[†]Key Laboratory of Plant Protection Resources & Pest Management of the Ministry of Education, College of Plant Protection, Northwest A&F University, Yangling, Shaanxi 712100, China

[‡]College of Horticulture and Plant Protection, Yangzhou University, Wenhui East Road, No. 48, Yangzhou, Jiangsu Province 225009, China

Supporting Information

ABSTRACT: *Grapholita molesta* is a notorious fruit borer globally, causing severe damage to fruit production. To control the pest, one commonly used mean is pheromone-mediated management. As an important sex pheromone, Z-8-dodecenyl acetate (Z8–12: Ac), is often coformulated with other active ingredients to regulate the behavior of *G. molesta*. To uncover its interactions with *G. molesta* pheromone binding protein 2 (GmolPBP2) is used to help develop insect attractants. During 200 ns molecular dynamics simulations, two representative conformations of the GmolPBP2-Z8–12: Ac complex are selected. Conformation II at the time of 14–106 ns is dominantly maintained by the hydrophobic interactions and hydrogen bond. In Conformation I, which lasts from 106 to 200 ns, the hydrophobic interactions are enhanced while the hydrogen bond is quite weakened, due to the formation of a more sophisticated hydrophobic binding pocket and the enlargement of hydrogen bond distance. Taking the two conformations as a whole, the affinity between GmolPBP2 and Z8–12: Ac is crucially determined by three hot-spots including Phe11, Trp36, and Ile51. These results would provide a basis for the discovery, optimization, and design of leading compounds potentially active to attract *G. molesta*.

KEYWORDS: *Grapholita molesta*, pheromone binding protein, sex pheromone, molecular simulations, site-directed mutagenesis

■ INTRODUCTION

The oriental fruit moth, *Grapholita molesta* (Busck), is a primary pest of stone and pome fruits in many fruit-growing countries.^{1,2} Its larvae are considered as notorious internal feeders in tender shoots and ripe fruits, causing severe damage to fruit production.^{3,4} During the growing season of *G. molesta*, host plant shift can be observed from stone fruits (peach, nectarine, etc.) to pome fruits (pear, apple, etc.).^{5,6} The pest has become an increasingly important fruit pest globally, especially in the interplanted areas of stone and pome fruits.²

The fruit- and shoot-boring habit makes the management of *G. molesta* difficult. Currently, this pest has been effectively controlled by use of broad-spectrum insecticides.^{7,8} However, the widespread use of conventional insecticides are often coupled with negative issues including insecticide resistance, food safety, and environmental pollution. In light of this, it would be useful to develop alternative control technologies able to cut down or even replace the usage of conventional insecticides.

In practice, pheromone-mediated management has been widely used in the mating disruption, mass trapping, monitoring, and forecasting of *G. molesta*.^{9–11} Previous studies show that the female sex pheromone of *G. molesta* is composed of Z-8-dodecenyl acetate (Z8–12: Ac), E-8-dodecenyl acetate (E8–12: Ac), Z-8-dodecenol (Z8–12: OH), and 1-dodecenol (12: OH).¹² However, only three of them (Z8–12: Ac, E8–12: Ac, and Z8–12: OH) are reported to be able to elicit male response.^{11,13} As a result, the three active ingredients are

coformulated and packaged as slow-release generator devices which are registered for use as mating disruptors or sexual attractants on *G. molesta*.^{14,15} Despite the excellent outcome in attracting *G. molesta*, the actual control effects of pheromone attractants in orchards are not always as good as expected. Such a negative consequence is a result of multiple factors, including unilateral attraction to male moths, multiple mating behaviors of male moth, stronger flight ability of female moths, and environmental conditions.^{16–18} Up until now, pheromone-mediated management is more commonly used as a supplementary measure of chemical control, and great improvements are required before it evolves to an alternative to conventional insecticide use globally.

Current attempts to develop novel attractants for pests are mainly focused on host-plant volatiles (HPVs). Many HPVs are reported to be able to attract insects as well as to enhance insect responses to sex pheromones.^{19–21} For *G. molesta*, two volatile compounds produced by peach plants, Z-3-hexenyl acetate and 1-undecanol, are capable of attracting the pest. Moreover, the addition of either Z-3-hexenyl acetate or 1-undecanol to the sex pheromone can significantly increase the attraction of traps baited with *G. molesta* sex pheromone alone.¹³ However, it should be noted that focusing only on

Received: January 3, 2019

Revised: March 11, 2019

Accepted: April 4, 2019

Published: April 4, 2019

HPVs is far from sufficient to optimize current situation of application of sexual attraction.

Insects rely on sensilla to perceive and transmit pheromone signals. In the signaling pathway of the pheromone, pheromone binding proteins (PBP) are thought to be indispensable. As a dominant PBP in the antenna sensilla of *G. molesta*, *G. molesta* pheromone binding protein 2 (GmolPBP2) is outstanding in binding with Z8-12: Ac, an essential ingredient of *G. molesta* sex pheromone.^{22,23} GmolPBP2 is consequently taken as a potential transporter of Z8-12: Ac. The main objective of the research is to describe the interaction modes between GmolPBP2 and Z8-12: Ac in detail. We started by generating a reliable model of the complex formed by GmolPBP2 and Z8-12: Ac. The two dominant conformations of the GmolPBP2-Z8-12: Ac complex in the 200 ns molecular dynamics (MD) simulations process were selected. After binding free energy workflows and computational alanine scanning (CAS) were used, the interactions and key residues involved in the two conformations were uncovered and compared. The results of molecular simulations were finally verified by biological tests. Unraveling the interaction details between GmolPBP2 and Z8-12: Ac would lay a solid foundation for the further discovery, optimization, and design of novel semiochemicals physiologically active to *G. molesta*.

MATERIALS AND METHODS

Homology Modeling of GmolPBP2. Homology modeling was performed by Modeler 9.10 to obtain the reliable 3D structure of GmolPBP2.²⁴ Taking the amino acid sequence of GmolPBP2 as a query, the crystal structure of *Amyelois transitella* pheromone binding protein 1 (AtraPBP1, PDB ID: 4INW, resolution = 1.14 Å) from the PDB95 database was chosen as the appropriate template for GmolPBP2 modeling.²⁵ The steps involved in the construction and refinement of GmolPBP2 3D model were in line with our former reports.^{26,27} Based on the 3D structure of the selected template, 100 3D models of GmolPBP2 protein were automatically generated by the automodel module of Modeler 9.10. After the initial optimization using the variable target function method (VTFM) with conjugate gradients (CG), each 3D model was subjected to molecular dynamics (MD) with simulated annealing (SA) for further refinement. Besides, the conformations of the loops in each 3D model were also refined by the loopmodel class in Modeler software. Finally, to measure the relative stability of GmolPBP2 conformations, the refined 3D models were checked by the GA341 and the discrete optimized protein energy (DOPE) scores. The one equipped with the lowest DOPE energy was determined as the credible 3D structure of GmolPBP2 protein. After all that, the quality of the final 3D model for further study was assessed by MolProbity and Profile 3D.^{27,28}

GmolPBP2-Z8-12: Ac Complex Construction. GOLD 5.3 software was used to construct the complex formed by GmolPBP2 and Z8-12: Ac.²⁹ The 3D structure of the Z8-12: Ac molecule was sketched using Maestro and optimized for 2000 steps with the GAFF force field in Amber12.^{30,31} As the acceptor for docking simulations, the final 3D model of GmolPBP2 produced by homology modeling was subjected to Amber12 for energy minimization (5000 steps) with the ff9SB force field.^{31,32} After that, the active pocket of GmolPBP2 was predicted using the Ligandscout v4.2.2 software, and the pocket grid was defined as the binding site. Considering the superiority of ChemPLP in predicting binding pose, ChemPLP, instead of other scoring functions in the GOLD 5.3 software, was employed to obtain the most accurate binding modes for the GmolPBP2-Z8-12: Ac complex.^{27,33,34} Visualization of the structures was performed by PyMol version 1.3.³⁵

Molecular Dynamics (MD) Simulations. The 200 ns MD simulations of the GmolPBP2-Z8-12: Ac complex were implemented with three replications by Amber12 package.³¹ For the complex

formed by GmolPBP2 and Z8-12: Ac, parameters and charges of the ligand Z8-12: Ac were set according to the GAFF and AMI-BCC method,^{30,36} while parameters for the ligand-acceptor GmolPBP2 were determined using the bioorganic systems force field (ff9SB) provided by the Amber software.³² The 3D structure of the GmolPBP2-Z8-12: Ac complex was immersed in a rectangular box with explicit TIP3P water extending at least 8 Å in each direction from the solute, and Na⁺ ions were added to maintain the neutrality of the system. To eliminate unfavorable contacts, energy of the GmolPBP2-Z8-12: Ac complex was minimized by the steepest descent method for the first 5000 steps and by the conjugate gradient method for the subsequent 5000 steps.

The MD simulations of the target complex can be divided into two phases. In the equilibration phase, the solvated complex was handled slowly as follows: heating in the NVT ensembles from 0 to 300 K in 500 ps, density equilibration with weak restraints for 500 ps, and constant pressure with unrestrained equilibration at 300 K for 5 ns. As for the production phase, it was run for 200 ns in the same conditions as the equilibration phase to prevent an abrupt jump in the potential energy. The coordinates were recorded every 10 ps so that the produced structures were of sufficient irrelevance. Both equilibration and production phases proceeded in the isothermal isobaric (NPT) ensemble using a Berendsen barostat.³⁷

The GmolPBP2-Z8-12: Ac complex trajectories in the 200 ns MD simulations were clustered using the average-linkage algorithm. The MD results were analyzed by the Ambergtools12 package.³¹ All the details of MD simulations were performed according to our previous reports.^{26,33,38,39}

Binding Free Energy Calculation. The theoretical binding free energy values ($\Delta G_{\text{bind-cal}}$) of the two representative conformations of the GmolPBP2-Z8-12: Ac complex in the 200 ns MD simulations were calculated by the molecular mechanics-Poisson-Boltzmann surface area (MM-PBSA) method in Amber12 software.⁴⁰ To calculate the theoretical binding free energy more accurately, the entropy contributions ($T\Delta S$) derived from changes in the translational, rotational, and vibrational degrees of freedom were considered as well. In the present research, $T\Delta S$ was calculated using normal-mode by the nmode program in Amber12.⁴¹ Detailed procedures were similar to our former studies.^{34,42}

Per-Residue Free Energy Decomposition. To quantify the binding free energy contribution of each residue in the two MD representative conformations of GmolPBP2-Z8-12: Ac complex, per-residue free energy decomposition was implemented by the MM-PBSA method incorporated in Amber12 software.⁴³ The residue contribution was depicted from the side-chain energy contribution, the backbone energy contribution, and the total energy contribution. As for the three energy contributions listed above, each of them were calculated on the basis of three energy items, including van der Waals energy, electrostatic energy, and polar-solvation free energy. Details were in accordance with former studies.^{26,42}

Computational Alanine Scanning. As a reliable technology to predict warm- and hot-spots associated with protein-protein or protein-ligand interaction, computational alanine scanning (CAS) was used to determine residues key to the GmolPBP2-Z8-12: Ac interactions.⁴⁴ In our research, residues contributing more than -1.00 kcal/mol binding free energy were subjected to CAS. The calculated binding free energy changes ($\Delta\Delta G_{\text{bind-cal}}$) caused by the mutation were calculated by the MM-PBSA method. Details of CAS were similar to our former reports.^{33,34,42}

Site-Directed Mutagenesis. The site-directed mutation of GmolPBP2 proceeded according to the manual book of a site-directed mutagenesis kit (Vazyme). Residues for the mutation were determined on account of CAS. Primers used for the mutation were designed as required and listed in Table S1.

Competitive Binding Assay. The wildtype and mutant GmolPBP2 genes were cloned into the pCold III vector (TaKaRa) and expressed in TransB (DE3, Transgen) *E. coli* cells. Details related to the protein expression and purification were shown in the Supporting Information. The binding ability changes that arose from

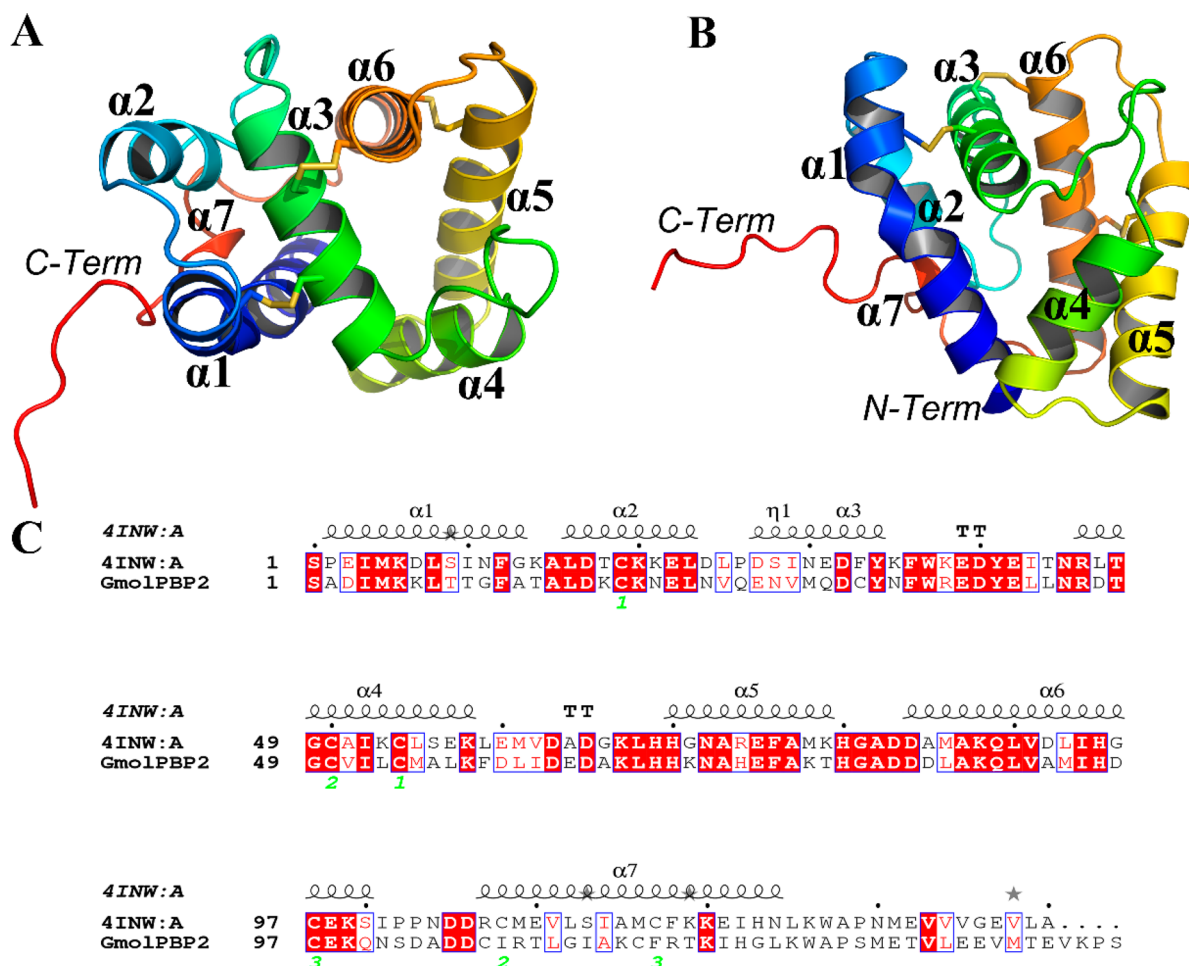


Figure 1. Structure of GmolPBP2. (A, B) The stereo views of GmolPBP2. (C) The amino acid sequences alignment of GmolPBP2 and AtraPBP1. The seven α -helices in GmolPBP2 are marked as $\alpha 1$ – $\alpha 7$. C-Term and N-Term are abbreviations for C-terminus and N-terminus, respectively. 4INW:A represents the AtraPBP1.

the site-directed mutation were measured by competitive binding assays, and tests at each point were performed in three repetition.

In the competitive binding assay, 1-NPN was used as the fluorescent probe. First, 2 μ M wildtype and mutant GmolPBP2 proteins were individually dissolved in the 10 mM PBS (pH 7.4) solutions plus 2 μ M 1-NPN. The prepared mixtures were titrated with 1 mM Z8–12: Ac dissolved in methanol of GC grade, with the final concentrations of Z8–12: Ac ranging from 0 to 64 μ M. To figure out the dissociation constant (K_d) between wildtype/mutant GmolPBP2 proteins and 1-NPN, 2 μ M target proteins dissolved in 10 mM PBS (pH 7.4) were titrated with 1 mM 1-NPN methanol solution to final concentrations of 0.5–30 μ M. Fluorescence responses were detected by a Hitachi F-4600 spectrofluorometer, where the excitation wavelength was set as 337 nm and the emission spectra were recorded between 350 and 500 nm. Detail procedures were similar to former research.⁴⁵

Statistics. The data of competitive binding assay were analyzed by GraphPad Prism 6.0 (Graphpad Software, Inc.). The K_d values between GmolPBP2 proteins (including wildtype and mutant GmolPBP2 proteins) and Z8–12: Ac were calculated according to eq 1.

$$K_d = IC_{50} / (1 + [1 - NPN] / K_{1-NPN}) \quad (1)$$

In eq 1, IC_{50} is the ligand concentration where the ligand quenches the fluorescence intensity of 1-NPN to 50%; $[1-NPN]$ represents the free concentration of 1-NPN, and K_{1-NPN} stands for the K_d of the GmolPBP2-Z8–12: Ac complex. The details of the K_d calculation are in accordance with our former report.⁴⁵

To compare the results of CAS and competitive binding assays, the obtained K_d values were further transformed into experimental binding free energy changes ($\Delta\Delta G_{\text{bind-exp}}$) using eq 2.⁴⁴

$$\Delta\Delta G_{\text{bind-exp}} = RT \ln(K_{d-MT} / K_{d-WT}) \quad (2)$$

In eq 2, R and T represent the ideal gas constant and the temperature in Kelvin, respectively; K_{d-MT} and K_{d-WT} are the K_d values between the mutant and wildtype GmolPBP2 proteins and Z8–12: Ac, respectively.

RESULTS AND DISCUSSION

3D Structure of GmolPBP2. In view of the R factor (0.16) and amino acid sequence identity (54%), AtraPBP1 was taken as the template for homology modeling. After the construction and optimization by Modeler 9.10 software, the final 3D model of GmolPBP2 was further checked. For all the 141 residues included in the 3D structure of GmolPBP2, the Ramachandran plot (Figure S2) shows that 97.2% (137/141) are in favored (98%) regions and 100% (141/141) are in allowed (>99.8%) regions. Meanwhile, the verification by Profile 3D (Figure S3) reveals that 91.61% residues in the 3D model have an average 3D-1D score ≥ 0.2 , and at least 80% residues score ≥ 0.2 in the 3D/1D profile. Both results from the Ramachandran plot and Profile 3D indicate the stereochemical rationality of the constructed GmolPBP2 model.

As shown in Figure 1, the 3D model of GmolPBP2, which consists of seven α -helices, is roughly arranged in a conical form. Moreover, three disulfide bonds are formed by the six conserved cysteine residues to connect $\alpha 1$ and $\alpha 3$ (Cys19-Cys54), $\alpha 3$ and $\alpha 6$ (Cys50-Cys107), and $\alpha 5$ and $\alpha 6$ (Cys96-Cys115). The formation of disulfide bonds helps to hold the 3D structure of GmolPBP2 and the active pocket where target ligand binds. Comparing with the 3D structures of most insect PBPs, GmolPBP2 is distinguished from most insect PBPs (usually consists of six α -helices) by the extra small α -helix ($\alpha 7$) at the C-terminus.^{25,46,47} Considering the conformational changes of C-terminal tails in the pheromone binding and release of insect PBPs, the distinctive seventh α -helix at C-terminus may contribute to the unique binding profiles of GmolPBP2.^{48,49}

MD Simulations of the GmolPBP2-Z8-12: Ac Complex. As shown in Figure S4, the section marked red in the 3D model of GmolPBP2 was determined to be the site where Z8-12: Ac binds. The GmolPBP2-Z8-12: Ac complex was generated by docking the Z8-12: Ac molecule into the red section. In the course of 200 ns MD simulations, the optimized GmolPBP2-Z8-12: Ac complex equilibrates rapidly at about 25 ns, with an averaged root-mean-square deviation (RMSD) of 3.28 ± 0.23 Å (Figure 2A). After a brief wild fluctuation, the ligand Z8-12: Ac in the complex achieves equilibration at the

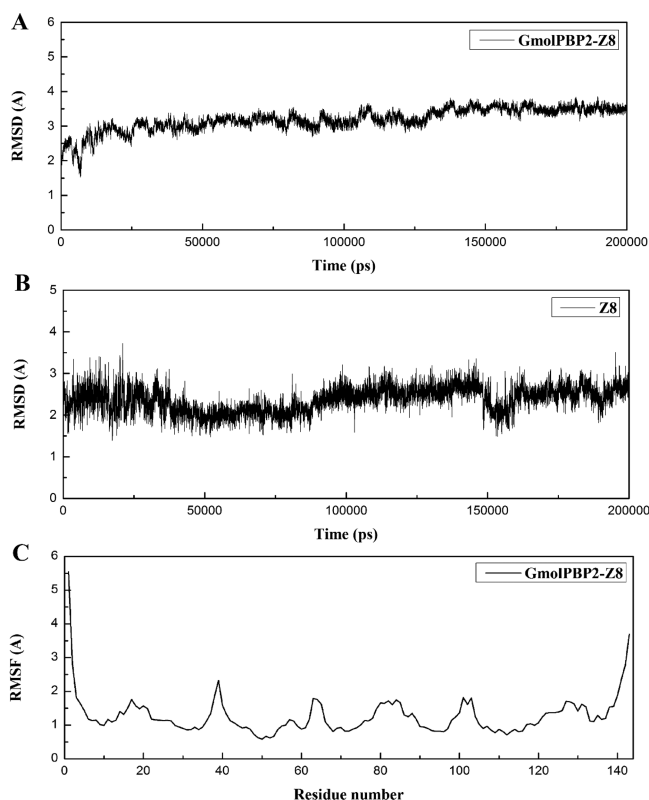


Figure 2. Molecular dynamics (MD) simulations (200 ns) of the GmolPBP2-Z8-12: Ac complex. (A) RMSD values for the GmolPBP2-Z8-12: Ac complex during the 200 ns MD simulations. (B) RMSD values for the Z8-12: Ac molecule during the 200 ns MD simulations. (C) Residue fluctuations for the GmolPBP2-Z8-12: Ac complex during the 200 ns MD simulations. GmolPBP2-Z8 and Z8 represent the GmolPBP2-Z8-12: Ac complex and Z8-12: Ac, respectively. As supporting information, the results of another two repetitions of MD simulations are shown in Figure S4.

time point of 50 ns, with an RMSD of 2.39 ± 0.29 Å (Figure 2B). The results of the three repetitions of MD simulations were proved to be highly consistent (Figures 2 and S5).

Root-mean-square fluctuation (RMSF) helps to uncover the flexibility and local motion characters of the secondary structure elements of GmolPBP2 on the binding of Z8-12: Ac. It is clear in Figure 1 that the 3D model of GmolPBP2 is composed of α -helices and free loops. In the figure of RMSF (Figure 2C), the six relatively sharp peaks correspond to the six loops between the seven α -helices in the 3D structure of GmolPBP2 (Figure 1). It is evident that the loop regions are much more flexible than the coiled regions. Although wild RMSF fluctuations are detected at the two termini (N-terminus and C-terminus) of GmolPBP2, their spatial distances to the binding site of Z8-12: Ac are too far away to shed negative effects on the stability of the GmolPBP2-Z8-12: Ac complex. The analysis of RMSD and RMSF in the course of 200 ns MD simulations indicates the rationality and stability of the GmolPBP2-Z8-12: Ac complex.

Binding Mode Analysis of the GmolPBP2-Z8-12: Ac Complex. The GmolPBP2-Z8-12: Ac complex trajectories collected during the 200 ns MD simulations were clustered using the average-linkage algorithm and the pairwise RMS. Of the five produced clusters (Cluster I–IV) listed in Figure S6 and Table S2, the Cluster I and Cluster II are two representative clusters with high occupancy. For Cluster I (47.1% occupancy), it persists from the time point of 106 to 200 ns. As shown in the MD representative conformation of Cluster I (Conformation I for short), the ligand Z8-12: Ac located in the hydrophobic pocket consists of residues that include Phe11, Phe35, Trp36, Ile51, Ile93, and Phe116, of which only Trp36 are polar residues (Figure 3A). A hydrogen

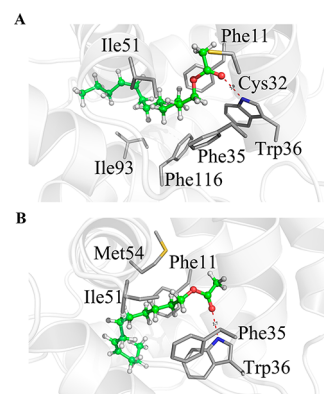


Figure 3. Key interactions at the active sites of the two representative conformations of the GmolPBP2-Z8-12: Ac complex. (A) The interactions derived from the representative conformation of Cluster I. (B) The interactions derived from the representative conformation of Cluster II. For each conformation, Z8-12: Ac is shown as a stick-and-sphere model. C atom, green sphere; O atom, red sphere; N atom, blue; S atom, gold; hydrogen bond, red dashed lines. In (A) and (B), the distances of hydrogen bonds are 3.0 and 2.7 Å, respectively.

bond is detected between the NZ atom of Trp36 and the O atom from the ACE (acetoxyl) of Z8-12: Ac, with the N–O distance of 3.0 Å and the hydrogen bond angle of 154.13°. As the only hydrophilic residue in the pocket, the polar Cys32 which dissociates itself from the formation of disulfide bond contributes to the binding of Z8-12: Ac as well. As Figure 3A shows, just because of the polarity, the S atom from the side-

Table 1. Theoretical Binding Free Energy^a for the Binding of Z8-12: Ac to the GmolPBP2

cluster	ΔE_{ELE}	ΔE_{VDW}	ΔE_{EGB}	ΔE_{SURF}	ΔG_{GAS}	ΔG_{SOL}	$-T\Delta S_{\text{TOT}}$	$\Delta G_{\text{bind-cal}}^b$	$\Delta G_{\text{bind-abs}}^c$
I	-1.76(0.039)	-41.23(0.082)	6.23(0.044)	-5.94(0.008)	-42.99(0.092)	0.29(0.046)	23.16(0.75)	-42.70(0.10)	-19.54
II	-8.15(0.079)	-42.24(0.092)	11.73(0.047)	-5.95(0.009)	-50.39(0.12)	5.78(0.048)	20.94(0.75)	-44.62(0.12)	-23.68

^aAll values are given in kcal/mol, with corresponding standard errors of the mean in parentheses. ^bThe theoretical binding free energy without considering entropy effect. ^cThe absolute theoretical binding free energy considering entropy effect.

chain of Cys32 forms a polar interaction with the ACE of Z8-12: Ac.

The Cluster II (46.0%), whose occupancy approximates to that of Cluster I, is kept from 14 to 106 ns in terms of the 200 ns MD simulations. In the MD representative conformation of Cluster II (Conformation II for short), the ligand Z8-12: Ac resides in the hydrophobic pocket composed of Phe11, Phe35, Trp36, and Ile51 (Figure 3B). The hydrogen bond shown in Figure 3A is also detected at the same site of Conformation II, with a closer N–O distance of 2.7 Å and a wider hydrogen bond angle of 157.25° (Figure 3B). Notably, the polar interaction derived from the side-chain of Cys32 in Conformation I is replaced by the counterpart contributed by Met54. As displayed (Figure 3B), the methylthio of the hydrophilic Met54 side-chain can form a significant polar interaction with the ACE of Z8-12: Ac.

As a whole, besides the significant van der Waals interactions, the hydrogen bond provided by Trp36 plus the polar interactions contributed by sulfur-bearing hydrophilic residues including Cys32 and Met54 also play a role in the binding of Z8-12: Ac to the hydrophobic pocket of GmolPBP2.

Binding Free Energy Calculation. Calculating the theoretical binding free energy of ($\Delta G_{\text{bind-cal}}$) the protein–ligand complex helps to further evaluate the reliability of molecular docking and binding mode analysis. In the present research, the MM-PBSA approach was employed to calculate the $\Delta G_{\text{bind-cal}}$ of the two representative conformations (Conformations I and II) during the time scope of the MD simulations. It should be noted that the standard error of mean (SEM) of each energy item listed in Table 1 is within 0.10 kcal/mol, indicating the reliability of the $\Delta G_{\text{bind-cal}}$ calculated in Table 1. For Conformation I, the hydrophobic interactions ($\Delta E_{\text{VDW}} = -41.23$ kcal/mol) contribute significantly to the binding of Z8-12: Ac to GmolPBP2 (Table 1). The electrostatic interaction contribution ($\Delta E_{\text{ELE}} = 1.76$ kcal/mol) is fairly weak (Table 1), in spite of the hydrogen bond detected in Conformation I (Figure 3A). The solvation free energy can be divided into two parts, with the nonpolar part (ΔE_{SURF}) providing favorable contribution and polar part (ΔE_{EGB}) providing unfavorable contribution. As is shown in Table 1, the ΔE_{SURF} and ΔE_{EGB} contributions in Conformation I are -5.94 and 6.23 kcal/mol, respectively. To calculate the $\Delta G_{\text{bind-cal}}$ accurately, the effects caused by conformational entropy changes ($-T\Delta S$) are necessarily of concern. In Conformation I, the $-T\Delta S$ value is determined to be 23.16 kcal/mol (Table 1). As a result, the absolute theoretical binding free energy ($\Delta G_{\text{bind-abs}}$) for Conformation I of the GmolPBP2-Z8-12: Ac complex should be calculated as -19.54 kcal/mol, rather than -42.70 kcal/mol (Table 1).

For Conformation II, the binding free energy contributions of most items in Table 1 are quite different from the counterparts of Conformation I. As shown (Table 1), the hydrophobic interactions remain as the major driving forces in Conformation II, with a ΔE_{VDW} value of -42.24 kcal/mol.

Notably, the favorable ΔE_{ELE} of Conformation II is as high as -8.15 kcal/mol, approximately five times that of Conformation I. The polar and nonpolar parts of solvation free energy react differently on the conformational changes of the GmolPBP2-Z8-12: Ac complex. Compared with the counterparts in Conformation I, the ΔE_{SURF} in Conformation II (-5.95 kcal/mol) presents very little change, whereas ΔE_{EGB} is almost doubled (11.73 kcal/mol). Consequently, the energy contributions of favorable ΔG_{GAS} ($\Delta E_{\text{ELE}} + \Delta E_{\text{VDW}}$) and unfavorable ΔG_{SOL} ($\Delta E_{\text{SURF}} + \Delta E_{\text{EGB}}$) arrive at -50.39 and 5.78 kcal/mol, respectively. As for the $-T\Delta S$, it decreases from the 23.16 kcal/mol in Conformation I to 20.94 kcal/mol in Conformation II. So, the $\Delta G_{\text{bind-abs}}$ for Conformation II of the GmolPBP2-Z8-12: Ac complex is finally calculated to be -23.68 kcal/mol.

Comparing the results of binding free energy calculation and binding mode analysis, it can be speculated that the interactions key to the formation of GmolPBP2-Z8-12: Ac complex, either in Conformation I or Conformation II, all contribute significantly to the absolute theoretical binding free energy. Such consistency of binding free energy calculation and binding mode analysis suggests the dependability of the 200 ns MD simulations.

Per-Residue Free Energy Decomposition. To quantify the free energy contribution of each residue in GmolPBP2, MM-PBSA was used to perform the per-residue free energy decomposition of Conformation I and Conformation II (Figure 4, Table 2). In Conformation I, Phe11, Cys32, Phe35, Ile51, Ile93, and Phe116 are residues contributing more than -1.00 kcal/mol total free energy to the binding of Z8-12: Ac (Figure 4A, Table 2). For Phe11 and Ile51 in particular, their total free energy contributions even exceed -2.00 kcal/mol. Residues including Phe11, Phe35, Ile51, Ile93, and Phe116 are suggested to be involved in forming the hydrophobic pocket where Z8-12: Ac binds (Figure 3A). As expected, these hydrophobic residues all provide beyond -1.00 kcal/mol van der Waals energy (T_{VDW}). Thereinto, the S_{VDW} of Phe11 even achieves -2.39 kcal/mol. For Ile51, it is highlighted by the striking S_{VDW} (-1.84 kcal/mol) as well as the relatively high van der Waals energy derived from its backbone ($B_{\text{VDW}} = -0.49$ kcal/mol). Although Trp36 (NZ atom) is the residue forming the hydrogen bond with the O atom from the ACE of Z8-12: Ac (Figure 3A), its electrostatic energy ($T_{\text{ELE}} = -0.47$ kcal/mol), represented by the energy of the hydrogen bond, is fairly low (Table 2). Such a consequence can be attributed to the larger N–O distance (3.0 Å) and the narrower hydrogen bond angle (154.13°) in Conformation I (Figure 3A). Not only that, the Trp36 side-chain also provides 0.87 kcal/mol polar solvation energy (S_{EPB}), which is unfavorable to the binding of Z8-12: Ac. As a consequence, the total interaction free energy (T_{TOT}) of Trp36 is only -0.79 kcal/mol, even though its S_{VDW} is in excess of -1.00 kcal/mol (Table 2). It is worth noting that, due to the polarity and electrostatic interaction ($T_{\text{ELE}} = -0.39$ kcal/mol), Cys32 is a residue whose energy contribution exceeds -1.00 kcal/mol as

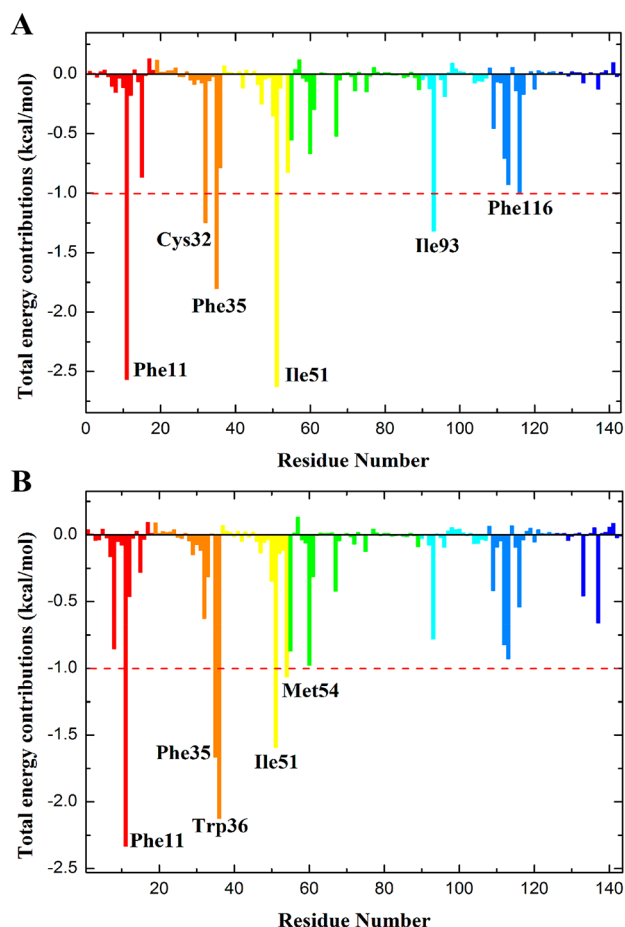


Figure 4. Residue–ligand interaction spectra of the two representative conformations of the GmolPBP2-Z8–12: Ac complex. The Y-axes denote the total binding free energy contributions of each residue in the representative conformations of Cluster I (A) and Cluster II (B), and the X-axes represent the residue number of GmolPBP2. In the two conformations, residues contributing more than -1.00 kcal/mol binding free energy are marked.

well (Figure 4A). Not only that, the polar nature of Cys32 also results in the relatively higher van der Waals energy ($T_{VDW} = -1.20$ kcal/mol), even though Cys32 is a hydrophilic residue. The same as a residue containing an S atom in its side-chain, the binding free energy contribution of Met54 ($T_{TOT} = -0.83$ kcal/mol) is much weaker than that of Cys32 ($T_{TOT} = -1.25$ kcal/mol).

In Conformation II, the residues contributing total free energy (T_{TOT}) above -1.00 kcal/mol are five in total, namely, Phe11, Phe35, Trp36, Ile51, and Met54 (Figure 4B, Table 2). Of the five residues, Phe11 and Trp36 are highlighted by their T_{TOT} values of more than -2.00 kcal/mol. Compared with the T_{TOT} (-2.04 kcal/mol) of Phe11 in Conformation I, the counterpart in Conformation II goes through a slight increase ($T_{TOT} = -2.33$ kcal/mol), despite the relatively higher unfavorable polar solvation energy (Table 2). The reason for the increase of T_{TOT} in Conformation II can be generally attributed to the electrostatic energy provided by Phe11 ($T_{ELE} = -0.37$ kcal/mol) as well as the extra van der Waals energy derived from the Phe11 backbone ($B_{VDW} = -0.45$ kcal/mol). The total electrostatic energy of Trp36 is dominantly contributed by the side-chain. On account of the shorter hydrogen bond distance (2.7 Å in Conformation II vs 3.0 Å in Conformation I) and the wider hydrogen bond angle (157.25°), the S_{ELE} of Trp36 in Conformation II, represented by the energy of the hydrogen bond, is as high as -2.60 kcal/mol, multi-fold higher than the counterpart in Conformation I (Table 2). Meanwhile, the unfavorable S_{EPB} derived from the Trp36 side-chain is more than doubled in Conformation II (1.84 kcal/mol vs 0.87 kcal/mol). The total free energy contributions of Phe35 and Ile51 in Conformation II are decreased in different degrees. Especially for Ile51, its T_{TOT} is lowered by 1.00 kcal/mol, due to the reduction of S_{VDW} by 0.80 kcal/mol and the increase of unfavorable B_{EPB} by 0.12 kcal/mol (Table 2). In Conformation II, the energy contributions of Cys32, Ile93, and Phe116 are reduced below -1.00 kcal/mol, while the energy contribution of Met54 goes up to -1.06 kcal/mol. As Table 2 shows, the augment of total free energy of Met54 can be attributed to its

Table 2. Results of Per-Residue Free Energy Decomposition^a

time scope	residue	S_{VDW}	B_{VDW}	T_{VDW}	S_{ELE}	B_{ELE}	T_{ELE}	S_{EPB}	B_{EPB}	T_{EPB}	S_{TOT}	B_{TOT}	T_{TOT}
106–200 ns	Phe11	-1.93	-0.037	-2.39	-0.091	0.010	-0.081	0.40	-0.083	0.197	-1.91	-0.13	-2.04
	Cys32	-0.65	-0.55	-1.20	-0.37	-0.024	-0.39	0.13	0.33	0.46	-0.97	-0.27	-1.25
	Phe35	-1.48	-0.10	-1.58	-0.18	-0.02	-0.20	-0.08	0.16	-0.11	-1.85	0.04	-1.80
	Trp36	-1.07	-0.04	-1.11	-0.44	-0.02	-0.47	0.87	0.003	0.87	-0.73	-0.06	-0.79
	Ile51	-1.84	-0.49	-2.33	0.03	-0.14	-0.11	-0.004	0.11	-0.30	-2.10	-0.53	-2.63
	Met54	-0.81	-0.11	-0.92	0.026	0.069	0.095	0.15	-0.082	0.068	-0.71	-0.12	-0.83
	Ile93	-0.97	-0.11	-1.09	0.009	-0.02	-0.014	-0.03	0.003	-0.03	-1.19	-0.13	-1.32
14–106 ns	Phe116	-1.04	-0.11	-1.15	0.009	0.05	0.062	0.22	-0.046	0.18	-0.90	-0.10	-1.00
	Phe11	-2.16	-0.45	-2.60	-0.18	-0.19	-0.37	0.39	0.49	0.88	-2.18	-0.15	-2.33
	Cys32	-0.52	-0.82	-1.34	-0.114	0.38	0.26	0.19	0.39	0.58	-0.54	-0.09	-0.63
	Phe35	-1.43	-0.11	-1.54	-0.23	-0.03	-0.25	0.11	0.12	0.23	-1.65	-0.02	-1.67
	Trp36	-1.18	-0.06	-1.24	-2.60	-0.05	-2.65	1.84	0.05	1.89	-2.07	-0.05	-2.12
	Ile51	-1.05	-0.59	-1.64	0.07	-0.07	0.002	-0.02	0.23	0.21	-1.14	-0.45	-1.59
	Met54	-0.84	-0.33	-1.17	0.04	0.06	0.10	0.07	0.04	-0.10	-0.83	-0.23	-1.06
Ile93	-0.55	-0.06	-0.61	0.012	-0.017	-0.005	-0.026	-0.007	-0.03	-0.70	-0.08	-0.78	
Phe116	-0.54	-0.05	-0.59	-0.022	0.023	-0.001	0.22	-0.08	0.14	-0.43	-0.11	-0.54	

^aEnergies are shown as contributions from van der Waals energy (VDW), electrostatic energy (ELE), polar solvation energy (EPB), and total energy (TOT) of side-chain atoms (S), backbone atoms (B), and the sum of them (T). All values are given in kcal/mol.

Table 3. Theoretical and Experimental $\Delta\Delta G_{\text{bind}}^a$ Values for the Complex Formed by Mutant GmolPBP2 Proteins and Z8–12: Ac

protein ^b	time scope	F11A	C32A	F35A	W36A	I51A	M54A	I93A	F116A
$\Delta\Delta G_{\text{bind-cal}}^c$	106–200 ns	3.10	1.25	4.32	2.54	4.12	1.64	2.57	2.17
	14–106 ns	4.30	0.37	3.25	5.46	2.53	1.07	1.27	1.41
$\Delta\Delta G_{\text{bind-exp}}^d$		5.78	1.70	3.75	6.89	4.78	1.19	2.91	1.47

^a $\Delta\Delta G_{\text{bind}}$ is the binding free energy change, and all values are given in kcal/mol. ^bF11A, C32A, F35A, W36A, I51A, M54A, I93A, and F116A are the abbreviations for GmolPBP2F11A, GmolPBP2C32A, GmolPBP2F35A, GmolPBP2W36A, GmolPBP2I51A, GmolPBP2M54A, GmolPBP2I93A, and GmolPBP2F116A, respectively. ^cThe theoretical $\Delta\Delta G_{\text{bind}}$ calculated by the MM-PBSA method. ^dThe experimental binding free energy changes ($\Delta\Delta G_{\text{bind-exp}}$) between the mutant and wildtype complexes are defined as $\Delta\Delta G_{\text{bind}} = RT \ln (K_{\text{d-MT}}/K_{\text{d-WT}})$, where R is the ideal gas constant and T is the temperature in Kelvin, and $K_{\text{d-MT}}$ and $K_{\text{d-WT}}$ are the K_{d} values between the mutant and wildtype GmolPBP2 proteins and Z8–12: Ac, respectively.

high van der Waals energy ($T_{\text{VDW}} = -1.17$ kcal/mol) and the fairly weak polar solvation energy.

Computational Alanine Scanning. CAS has been proved to be a reliable method for the determination of hot-spots and warm-spots in protein–ligand interaction. In the present research, CAS is consequently selected to predict key residues involved in the GmolPBP2-Z8–12: Ac interaction. In the two representative conformations of Cluster I and Cluster II, eight residues (Phe11, Cys32, Phe35, Trp36, Ile51, Met54, Ile 93, and Phe116) in total provide binding free energy of more than -1.00 kcal/mol (Table 2, Figure 4). As revealed by the theoretical binding free energy changes ($\Delta\Delta G_{\text{bind-cal}}$) listed in Table 3, the individual replacement of these residues by Ala causes negative effects of various degrees on the binding of Z8–12: Ac to GmolPBP2.

It is known that 2.00 and 4.00 kcal/mol are often used as cutoffs to define hot-spots, warm-spots, and null-spots. Residues for which alanine mutations cause an increase in the $\Delta\Delta G_{\text{bind-cal}}$ of at least 4.00 kcal/mol are defined as hot-spots. Warm-spots are residues with a $\Delta\Delta G_{\text{bind-cal}}$ value between 2.00 and 4.00 kcal/mol, and null-spots are those with a $\Delta\Delta G_{\text{bind-cal}}$ value lower than 2.00 kcal/mol.⁴⁴ As a consequence, only two residues in Conformation I, including Phe35 (4.32 kcal/mol) and Ile51 (4.20 kcal/mol), are predicted to be hot-spots (Table 3). Whereas in Conformation II, the hot-spots turn into Phe11 (4.30 kcal/mol) and Trp36 (5.46 kcal/mol). According to the results of free energy decomposition (Table 2), these hot-spots all contribute significant favorable energy ($T_{\text{TOT}} > -1.50$ kcal/mol), either van der Waals energy or electrostatic energy, to the GmolPBP2-Z8–12: Ac complex. To analyze Table 2 and Table 3 comprehensively, it can be found that all residues belonging to warm- and hot-spots are provided with a high side-chain free energy contribution ($S_{\text{TOT}} > -1.10$ kcal/mol). However, it should be noted that residues contributing high binding free energy are not necessarily hot-spots. Take the Phe11 ($\Delta\Delta G_{\text{bind-cal}} = 3.10$ kcal/mol) for example, it falls into the range of warm-spots in Conformation I (Table 3), even though its binding free energy contribution ($T_{\text{TOT}} = -2.04$ kcal/mol) is higher than that of the hot-spot Phe35 ($T_{\text{TOT}} = -1.80$ kcal/mol).

Competitive Binding Assay. The eight residues (Phe11, Cys32, Phe35, Trp36, Ile51, Met54, Ile93, and Phe116) contributing binding free energy more than -1.00 kcal/mol were individually mutated into Ala. Compared with the wildtype GmolPBP2, the eight mutant proteins all exhibit decreases of varying degree in binding with Z8–12: Ac (Figure 5). Especially for the three mutant GmolPBP2 proteins (GmolPBP2F11A, GmolPBP2W36A, and GmolPBP2I51A)

that correspond to the residues Phe11, Trp36, and Ile51, their dissociation constants (K_{d}) with Z8–12: Ac all increased more than six times (Figure 5A, D, E, I). Based on the K_{d} of each protein (wildtype and mutant GmolPBP2 protein) in Figure 5, the experimental binding free energy changes ($\Delta\Delta G_{\text{bind-exp}}$) caused by site-directed mutagenesis were calculated. As shown in Table 3, it is evident that the $\Delta\Delta G_{\text{bind-exp}}$ values of GmolPBP2F11A, GmolPBP2W36A, and GmolPBP2I51A proteins exceed 4.00 kcal/mol, suggesting that Phe11, Trp36, and Ile51 are three hot-spots for the GmolPBP2-Z8–12: Ac interactions. Whereas for other five residues, they are categorized into either warm-spots (Phe35 and Ile93) or null-spots (Cys32, Met54, and Phe116).⁴⁴ For the four hot-spots predicted by CAS (Phe11, Phe35, Trp36, and Ile51), three of them are verified to be right by competitive binding assay, with Phe35 being an exception (Table 3). Such a difference is acceptable; after all, the overall success of CAS in predicting hot-spots is about 80% rather than 100%. Of the three hot-spots, only one residue (Ile51) is derived from Conformation I (Table 3), indicating that Conformation II is more accurate in representing the interaction between GmolPBP2 and Z8–12: Ac. The statement can be laterally supported by the lower absolute binding free energy ($\Delta G_{\text{bind-abs}} = -23.68$ kcal/mol) in Conformation II (Table 1).

As a whole, the affinity between GmolPBP2 and Z8–12: Ac is crucially determined by three residues, namely, Phe11, Trp36 and Ile51, and their mutation into Ala can greatly decrease the ability of GmolPBP2 to bind with Z8–12: Ac (Table 3, Figure 5). In the dynamic process of forming the GmolPBP2-Z8–12: Ac complex, van der Waals interaction and electrostatic interaction are determined to be two dominant driving forces. Throughout the whole 200 ns MD simulations, Cluster II (between 14 and 106 ns) and Cluster I (between 106 and 200 ns) occurred consecutively (Table S2). In Conformation II, Phe11 and Trp36 are two key residues. Especially for Trp36, its existence is indispensable to anchor the molecule Z8–12: Ac into the binding pocket in Conformation II (Figure 3B, Table 3). At this stage, the hydrophobic interactions and hydrogen bond derived from the two residues are crucially important in the formation of the GmolPBP2-Z8–12: Ac complex (Figure 3B, Table 2). When it comes to Conformation I, the key residue to determine the GmolPBP2-Z8–12: Ac affinity turns into Ile51. In the conformation, a more sophisticated hydrophobic pocket is formed, suggesting that the GmolPBP2-Z8–12: Ac at this stage is dominantly maintained and stabilized by the enhanced hydrophobic interactions (Table 2, Figure 3A). As for the hydrogen bond interaction in Conformation I (Figure 3A), it becomes fairly weak due to the enlarged distance of N–O

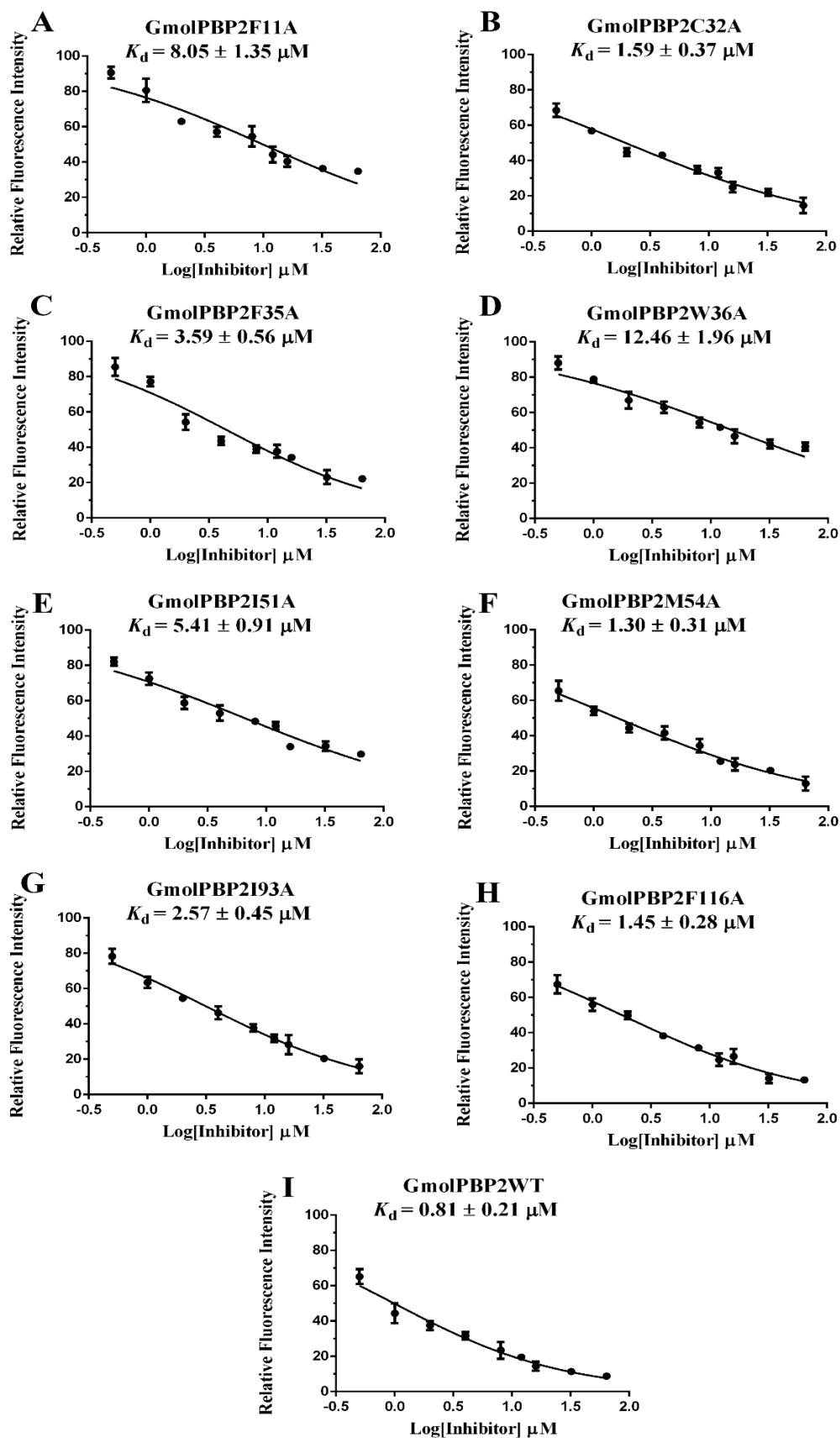


Figure 5. Binding curves of Z8-12: Ac to the mutant (A–H) and wildtype (I) GmolPBP2 proteins.

which is involved in the formation of the hydrogen bond, and the hydrogen bond is enlarged (Figure 3A).

In the present research, the interactions between GmolPBP2 and Z8-12: Ac are detailed through the integrated use of

molecular simulations and biological experiments. This information is necessary to realize the high-throughput virtual screening of novel insect attractants physiologically active to *G. molesta*. For example, as a technology commonly applied in high-throughput virtual screening, pharmacophore modeling requires the availability of such key interactions. Not only that, in light of the key interactions between GmolPBP2 and Z8–12: Ac, it is adequate to gain novel semiochemicals with better attracting effects by virtue of computer-aided drug design (CADD).

■ ASSOCIATED CONTENT

● Supporting Information

The Supporting Information is available free of charge on the ACS Publications website at DOI: 10.1021/acs.jafc.9b00052.

Determination of Z8–12: Ac as the target ligand; methods for protein expression and purification; selective analysis on the minor fluctuation at about 150 ns; supplements to the results of protein expression and competitive binding assay; superimposition of the 3D active conformations of Z8–12: Ac, E8–12: Ac, and Z8–12: OH (Figure S1); Ramachandran plot of the constructed 3D model of GmolPBP2 (Figure S2); 3D/1D profile of the constructed 3D model of GmolPBP2 (Figure S3); predicted binding sites of Z8–12: Ac in the active pocket of GmolPBP2 (Figure S4); two repetitions of the 200 ns MD simulations of the GmolPBP2–Z8–12: Ac complex (Figure S5); clusters produced during the 200 ns MD simulations (Figure S6); superimposition of the conformation of the GmolPBP2–Z8–12: Ac complex at about 150 ns and Conformation I (Figure S7); superimposition of the three corresponding Conformation I results derived from the three repetitions of 200 ns MD simulations (Figure S8); expression of wildtype and mutant GmolPBP2 proteins (Figure S9); binding curves between wildtype GmolPBP2 and Z8–12: Ac (Figure S10); primers for site-directed mutagenesis and protein expression (Table S1); and cluster analysis of the GmolPBP2–Z8–12: Ac complex based on the MD simulations trajectories (Table S2) (PDF)

■ AUTHOR INFORMATION

Corresponding Author

*E-mail: kinglly0818@hotmail.com.

ORCID

Jiyuan Liu: 0000-0002-3524-2064

Author Contributions

J.Y.L. and Z.T. conceived the project. J.Y.L. and Z.T. designed the experiment. Z.T., Y.L., Y.J.X., and R.C.L. performed the experiments and prepared the manuscript. J.Y.L. supervised the study and contributed the reagents and materials. All authors contributed to data analysis.

Funding

The research was supported by the Natural Science Foundation of Jiangsu Province (BK20180902), the National Natural Science Foundation of China (31801797), the Fundamental Research Funds for the Central Universities (2452018008), the Sci-Tech Planning Project of Yangling Demonstration Zone (2018NY-02), and the National Natural Science Foundation of China (21503272).

Notes

The authors declare no competing financial interest.

■ REFERENCES

- (1) Kirk, H.; Dorn, S.; Mazzi, D. Worldwide population genetic structure of the oriental fruit moth (*Grapholita molesta*), a globally invasive pest. *BMC Ecol.* **2013**, *13*, 12.
- (2) Neven, L. G.; Kumar, S.; Yee, W. L.; Wakie, T. Current and future potential risk of establishment of *Grapholita molesta* (Lepidoptera: Tortricidae) in Washington State. *Environ. Entomol.* **2018**, *47*, 448–456.
- (3) Myers, C. T.; Hull, L. A.; Krawczyk, G. Seasonal and cultivar-associated variation in oviposition preference of oriental fruit moth (Lepidoptera: Tortricidae) adults and feeding behavior of neonate larvae in apples. *J. Econ. Entomol.* **2006**, *99*, 349–358.
- (4) Rings, R. W. Economic aspects of the biology and control of the oriental fruit moth, *Grapholita molesta* Busck, in the United States. *Ohio J. Sci.* **1970**, *70*, 58–61.
- (5) Myers, C. T.; Hull, L. A.; Krawczyk, G. Effects of orchard host plants (apple and peach) on development of oriental fruit moth (Lepidoptera: Tortricidae). *J. Econ. Entomol.* **2007**, *100*, 421–430.
- (6) Najar-Rodriguez, A.; Orschel, B.; Dorn, S. Season-long volatile emissions from peach and pear trees *in situ*, overlapping profiles, and olfactory attraction of an oligophagous fruit moth in the laboratory. *J. Chem. Ecol.* **2013**, *39*, 418–429.
- (7) Atanassov, A.; Shearer, P. W.; Hamilton, G. C. Peach pest management programs impact beneficial fauna abundance and *Grapholita molesta* (Lepidoptera: Tortricidae) egg parasitism and predation. *Environ. Entomol.* **2003**, *32*, 780–788.
- (8) Jang, I.; Kim, H. M.; Lee, S. W.; Choi, K. H.; Suh, S. J. Analysis of pesticide applications on apple orchards in Geochang, Korea. *Korean J. Pestic. Sci.* **2015**, *19*, 93–100.
- (9) Rothschild, G. Control of oriental fruit moth (*Cydia molesta* (Busck) (Lepidoptera, Tortricidae)) with synthetic female pheromone. *Bull. Entomol. Res.* **1975**, *65*, 473–490.
- (10) Kang, Z. X.; Zhang, F. Y.; Sun, Q.; Lu, X.; Guo, M. Z. Application of sex attractant of *Grapholita molesta* for forecasting and control of *Grapholita funebrana*. *Insect Knowl.* **1989**, *26*, 142–145.
- (11) Kong, W. N.; Li, J.; Fan, R. J.; Li, S. C.; Ma, R. Y. Sex-pheromone-mediated mating disruption technology for the oriental fruit moth, *Grapholita molesta* (Busck) (Lepidoptera: Tortricidae): overview and prospects. *Psyche* **2014**, *2014*, 1.
- (12) Cardé, A.; Baker, T.; Cardé, R. Identification of a four-component sex pheromone of the female oriental fruit moth, *Grapholita molesta* (Lepidoptera: Tortricidae). *J. Chem. Ecol.* **1979**, *5*, 423–427.
- (13) Yu, H.; Feng, J.; Zhang, Q.; Xu, H. (Z)-3-hexenyl acetate and 1-undecanol increase male attraction to sex pheromone trap in *Grapholita molesta* (Busck) (Lepidoptera: Tortricidae). *Int. J. Pest Manage.* **2015**, *61*, 30–35.
- (14) Rothschild, G. A comparison of methods of dispensing synthetic sex pheromone for the control of oriental fruit moth, *Cydia molesta* (Busck) (Lepidoptera: Tortricidae), in Australia. *Bull. Entomol. Res.* **1979**, *69*, 115–127.
- (15) Padilha, A.; Arioli, C.; Boff, M.; Rosa, J.; Botton, M. Traps and baits for luring *Grapholita molesta* (Busck) adults in mating disruption-treated apple orchards. *Neotrop. Entomol.* **2018**, *47*, 152–159.
- (16) Il'ichev, A.; Hossain, M.; Jerie, P. Migration of oriental fruit moth *Grapholita molesta* Busck. (Lepidoptera: Tortricidae) under wide area mating disruption in Victoria, Australia. *IOBC wprs B* **1999**, *22*, 53–62.
- (17) Waldstein, D. E.; Gut, L. J. Effects of rain and sunlight on oriental fruit moth (Lepidoptera: Tortricidae) pheromone microcapsules applied to apple foliage. *J. Agr. Urban Entomol.* **2004**, *21*, 117–128.
- (18) Ellis, N. H.; Hull, L. A. Factors influencing adult male *Grapholita molesta* dispersal in commercial *Malus* and *Prunus* host crops. *Entomol. Exp. Appl.* **2013**, *146*, 232–241.

- (19) Varela, N.; Avilla, J.; Anton, S.; Gemeno, C. Synergism of pheromone and host-plant volatile blends in the attraction of *Grapholita molesta* males. *Entomol. Exp. Appl.* **2011**, *141*, 114–122.
- (20) Ammagarahalli, B.; Chianella, L.; Gomes, P.; Gemeno, C. Role of plant volatiles and hetero-specific pheromone components in the wind tunnel response of male *Grapholita molesta* (Lepidoptera: Tortricidae) to modified sex pheromone blends. *Bull. Entomol. Res.* **2017**, *107*, 573–582.
- (21) Barros-Parada, W.; Ammagarahalli, B.; Basoalto, E.; Fuentes-Contreras, E.; Gemeno, C. Captures of oriental fruit moth, *Grapholita molesta* (Lepidoptera: Tortricidae), in traps baited with host-plant volatiles in Chile. *Appl. Entomol. Zool.* **2018**, *53*, 193–204.
- (22) Song, Y.; Dong, J.; Qiao, H.; Wu, J. Molecular characterization, expression patterns and binding properties of two pheromone-binding proteins from the oriental fruit moth, *Grapholita molesta* (Busck). *J. Integr. Agric.* **2014**, *13*, 2709–2720.
- (23) Li, G.; Zhang, Y.; Li, Y.; Wu, J.; Xu, X. Cloning, expression, and functional analysis of three odorant-binding proteins of the oriental fruit moth, *Grapholita molesta* (BUSCK) (Lepidoptera: Tortricidae). *Arch. Insect Biochem. Physiol.* **2016**, *91*, 67–87.
- (24) Šali, A.; Blundell, T. L. Comparative protein modelling by satisfaction of spatial restraints. *J. Mol. Biol.* **1993**, *234*, 779–815.
- (25) di Luccio, E.; Ishida, Y.; Leal, W. S.; Wilson, D. K. Crystallographic observation of pH-induced conformational changes in the *Amyelois transitella* pheromone-binding protein AtrPBP1. *PLoS One* **2013**, *8*, e53840.
- (26) Tian, Z.; Liu, J.; Zhang, Y. Structural insights into *Cydia pomonella* pheromone binding protein 2 mediated prediction of potentially active semiochemicals. *Sci. Rep.* **2016**, *6*, 22336.
- (27) Liu, J.; Yang, X.; Zhang, Y. Characterization of a lambda-cyhalothrin metabolizing glutathione S-transferase CpGSTd1 from *Cydia pomonella* (L.). *Appl. Microbiol. Biotechnol.* **2014**, *98*, 8947–8962.
- (28) Chen, V. B.; Arendall, W. B.; Headd, J. J.; Keedy, D. A.; Immormino, R. M.; Kapral, G. J.; Murray, L. W.; Richardson, J. S.; Richardson, D. C. MolProbity: all-atom structure validation for macromolecular crystallography. *Acta Crystallogr., Sect. D: Biol. Crystallogr.* **2010**, *66*, 12–21.
- (29) Jones, G.; Willett, P.; Glen, R. C.; Leach, A. R.; Taylor, R. Development and validation of a genetic algorithm for flexible docking. *J. Mol. Biol.* **1997**, *267*, 727–748.
- (30) Wang, J.; Wolf, R. M.; Caldwell, J. W.; Kollman, P. A.; Case, D. A. Development and testing of a general amber force field. *J. Comput. Chem.* **2004**, *25*, 1157–1174.
- (31) Case, D. A.; Darden, T. A.; Cheatham, T. E., III; Simmerling, C. L.; Wang, J.; Duke, R. E.; Walker, R. C.; Zhang, W.; Merz, K. M.; et al. AMBER 12; University of California: San Francisco, CA, USA, 2012.
- (32) Hummer, G.; Rasaiah, J. C.; Noworyta, J. P. Water conduction through the hydrophobic channel of a carbon nanotube. *Nature* **2001**, *414*, 188.
- (33) Liu, J.; Li, Y.; Tian, Z.; Sun, H.; Chen, X. e.; Zheng, S.; Zhang, Y. Identification of key residues associated with the interaction between *Plutella xylostella* sigma-class glutathione S-transferase and the inhibitor S-hexyl glutathione. *J. Agric. Food Chem.* **2018**, *66*, 10169–10178.
- (34) Tian, Z.; Liu, J.; Zhang, Y. Key residues involved in the interaction between *Cydia pomonella* pheromone binding protein 1 (CpomPBP1) and Codlemone. *J. Agric. Food Chem.* **2016**, *64*, 7994–8001.
- (35) DeLano, W. L. The PyMOL molecular graphics system, version 1.3.0.4; Schrödinger LLC.: 2002.
- (36) Jakalian, A.; Jack, D. B.; Bayly, C. I. Fast, efficient generation of high-quality atomic charges. AMI-BCC model: II. Parameterization and validation. *J. Comput. Chem.* **2002**, *23*, 1623–1641.
- (37) Berendsen, H. J.; Postma, J. V.; van Gunsteren, W. F.; DiNola, A.; Haak, J. Molecular dynamics with coupling to an external bath. *J. Chem. Phys.* **1984**, *81*, 3684–3690.
- (38) Liu, J.; Tian, Z.; Zhang, Y. Structure-based discovery of potentially active semiochemicals for *Cydia pomonella* (L.). *Sci. Rep.* **2016**, *6*, 34600.
- (39) Liu, J.; Tian, Z.; Zhou, N.; Liu, X.; Liao, C.; Lei, B.; Li, J.; Zhang, S.; Chen, H. Targeting the apoptotic Mcl-1-PUMA interface with a dual-acting compound. *Oncotarget* **2017**, *8*, 54236–54242.
- (40) Hou, T.; Wang, J.; Li, Y.; Wang, W. Assessing the performance of the molecular mechanics/poisson boltzmann surface area and molecular mechanics/generalized born surface area methods. II. The accuracy of ranking poses generated from docking. *J. Comput. Chem.* **2011**, *32*, 866–877.
- (41) Kottalam, J.; Case, D. Langevin modes of macromolecules: applications to crambin and DNA hexamers. *Biopolymers* **1990**, *29*, 1409–1421.
- (42) Liu, J.; Chen, X.; Zhang, Y. Insights into the key interactions between human protein phosphatase 5 and cantharidin using molecular dynamics and site-directed mutagenesis bioassays. *Sci. Rep.* **2015**, *5*, 12359.
- (43) Gohlke, H.; Kiel, C.; Case, D. A. Insights into protein–protein binding by binding free energy calculation and free energy decomposition for the Ras–Raf and Ras–RalGDS complexes. *J. Mol. Biol.* **2003**, *330*, 891–913.
- (44) Moreira, I. S.; Fernandes, P. A.; Ramos, M. J. Computational alanine scanning mutagenesis—an improved methodological approach. *J. Comput. Chem.* **2007**, *28*, 644–654.
- (45) Tian, Z.; Zhang, Y. Molecular characterization and functional analysis of pheromone binding protein 1 from *Cydia pomonella* (L.). *Insect Mol. Biol.* **2016**, *25*, 769–777.
- (46) Sandler, B. H.; Nikonova, L.; Leal, W. S.; Clardy, J. Sexual attraction in the silkworm moth: structure of the pheromone-binding-protein–bombykol complex. *Chem. Biol.* **2000**, *7*, 143–151.
- (47) Mao, Y.; Xu, X.; Xu, W.; Ishida, Y.; Leal, W. S.; Ames, J. B.; Clardy, J. Crystal and solution structures of an odorant-binding protein from the southern house mosquito complexed with an oviposition pheromone. *Proc. Natl. Acad. Sci. U. S. A.* **2010**, *107*, 19102–19107.
- (48) Michel, E.; Damberger, F. F.; Ishida, Y.; Fiorito, F.; Lee, D.; Leal, W. S.; Wüthrich, K. Dynamic conformational equilibria in the physiological function of the *Bombyx mori* pheromone-binding protein. *J. Mol. Biol.* **2011**, *408*, 922–931.
- (49) Katre, U. V.; Mazumder, S.; Mohanty, S. Structural insights into the ligand binding and releasing mechanism of *Antheraea polyphemus* pheromone-binding protein 1: role of the C-terminal tail. *Biochemistry* **2013**, *52*, 1037–1044.